International Journal of Thin Films Science and Technology

http://dx.doi.org/10.12785/ijtfst/040108

Impact of Mole Concentration on the Structural and Optical Properties of Nebulized Spray Coated Cerium Oxide Thin Films

R. Suresh[1], *V. Ponnuswamy*[1,*] *and R. Mariappan*[2]

[1] Department of Physics, SRMV College of Arts and Science, Coimbatore, Tamil Nadu, India.
[2]Department of Physics, Athiyaman College of Engineering, Hosur, Tamil Nadu, India.

Received: 25 Jul. 2014, Revised: 3 Nov. 2014, Accepted: 8 Nov. 2014.

Abstract: Cerium oxide thin films are deposited on glass substrates with various mole concentrations by nebulized spray pyrolysis technique. The films are characterized for, XRD, SEM, AFM, FTIR, PL, UV-ViS and XPS. All films exhibit cubic fluorite structure with preferred orientations along (200) direction with an average size of 30 nm. The films exhibit dense, smooth and crack-free spherical like tiny particles composed of nanostructures with some uneven size 52 nm. It also exhibits nicely separated conical columnar microstructure. FT-IR analysis confirm the presence of (Ce=O) terminal stretching and phonon band (Ce-O) of metal oxide network. PL analysis indicates the presence of indigo and yellow emission in the visible region centered on ~425 and ~579 nm respectively. UV-ViS spectra reveal that the films are transparent (60%) in the visible region. Optical parameters like refractive index, optical conductivity and band gap are calculated for different mole concentrations. XPS analysis reveals the existence of Ce, O and C and the dominant occurrence of Ce^{4+} rather than Ce^{3+} in the films.

Keywords: Cerium oxide, Emission properties, XPS, Lattice constant, Optical conductivity, Cubic Fluorite.

1.Introduction

One of the most abundant rare earth ionic compounds ceria has generated enormous attention owing of its high chemical stability, good dielectric strength, high refractive index, good optical transmittance in the visible and infrared regions and high efficiency for absorbing ultraviolet radiation. It also exhibits a high stability against mechanical abrasion and chemical erosion due to its strong adhesion to surfaces [1]. It exhibit cubic fluorite structure (Face Centered Cubic) in which each cerium site is surrounded by eight oxygen sites in FCC arrangement and each oxygen site has a tetrahedron cerium site. It can accommodate both intrinsic and extrinsic oxygen vacancies and thus it may act as an oxide ion conducting material [2]. Intrinsic vacancies are formed by the presence of Ce (III) ions in the fluorite lattice due to the reduction equilibrium of Ce^{4+}/Ce^{3+}, whereas extrinsic vacancies are arisen by substitution of ions in the lattice. It exhibits two structures mainly cubic fluorite cerium dioxide or ceria (due to tetravalent Ce) and a hexagonal sesquioxide Ce_2O_3 (due to trivalent Ce) [3]. Spray pyrolyzed thin films offer high film quality and low processing costs compared with other conventional thin film preparation techniques like pulsed laser deposition, chemical or physical vapor deposition. It involves the atomization of a liquid precursor containing metal salts, droplet transport towards a heated substrate and film formation on the substrate surface, evaporation of the solvent and decomposition of the deposited material [4]. Crack-free films are obtained when deposition temperature is above precursor boiling point (290°C). The degree of decomposition is determined by the relationship among the substrate temperature, boiling point of the solvents and melting pointing points of the salts used to the precursor [5].

Ceria based thin films can be employed as an intermediate buffer layer in fuel cells [6-8], electrochemical devices [9-12], optoelectronic devices [13], Photo-catalytic activity [14,15], Flat panel displays [16] and gas sensors [17-19]. Traditional preparation methods of ceria-based thin films include CVD (Chemical Vapor Deposition) [20], Pulsed Laser Deposition [21], Dip coating [22], ESAVD (Electrostatic Spray Assisted Vapor Deposition) [23], Sputtering [24-26], Flame Spray [27,28] and spray pyrolysis [3-5, 8,29].

This paper reports the structural, optical, compositional and electrical properties of cerium oxide thin films investigated for different mole concentrations.

2. Experimental Details

Cerium oxide thin films are deposited on glass substrates using cerium nitrate hexahydrate as the chemical precursor. The substrates are cleaned using hydrochloric acid, sodium hydroxide and isopropyl alcohol then rinsed with deionized

---

[*]Corresponding author e-mail: ponns007@yahoo.com

water. 0.02 M of cerium nitrate is dissolved in deionized water and stirred for 30 minutes. The prepared solutions are deposited on glass substrates with different mole concentrations (0.02 M to 0.1 M). Mole concentrations increase the film thickness. It plays a decisive role in structural, optical and surface properties. Compressed air is used as a carrier gas. Substrate temperature is maintained at 400^{o}C. The prepared samples are characterized by UV-Vis, PL, FT-IR, XRD, SEM, EDAX and XPS. In this method, the aerosol (cerium hydroxide) formed from nozzle undergoes successive pyrolysis due to temperature gradient, this successive pyrolysis results into decomposition of aerosol at substrate and leads to film formation. In case of CeO_2 film formation, the substrate temperature is fixed at 300^{o}C slightly higher than that of decomposition temperature (290^{o}C) of precursor solution.

In order to understand the properties of the materials, deep knowledge about the structure and their composition is important. X-ray diffraction (XRD) is a powerful technique used to identify the crystalline phases present in materials and measure the structural properties (strain state, grain size, epitaxy, phase composition, preferred orientation and defect structure) of these phases. Samples are analyzed by a XPERT-PRO, Bruker AXS D8 Advance X-ray diffractometer in the 0-90˚ (2θ) scale angle range. The thin film samples are analyzed using JEOL Model JSM - 6390LV instrument for high resolution surface imaging. Thin film samples are also analyzed using JEOL Model JED - 2300 instrument to identify the elemental composition. The surface morphology of the obtained nanocrystalline powder samples was taken as an image by scanning an area of 1 X 1 mm using an AFM (Atomic Force Microscope, NanosurfeasyScan 2, Switzerland) . Nanosurface roughness measurements were completed using an atomic force microscope and the NanosurfeasyScan 2 software. Commercially available AFM tips (detector side Al coating , thickness of the tip was 7 mm, tip length was 225 mm, tip width was 38 mm with a 48 N/ m force constant and 190 kHz resonance frequency) were used in intermittent contact (also called tapping) mode. Vibration stretching of cerium oxide thin films has been done with the help of IR spectra (PerkinElmer, model 783, USA) in the spectral range 700-4000 cm^{-1} with a resolution of 1 cm^{-1}. Photoluminescence (PL) measurements are measured on a Hitachi F-4500 FL spectrophotometer using a Xenon lamp as the excitation source at room temperature. The excitation wavelength is fixed at 325 nm. Optical characterization of thin film is mainly done by taking absorption, transmittance and reflection with the help of optical spectrophotometer in a range of wavelengths. The optical properties of CeO_2 thin films are investigated by computer controlled UV-Visible spectrophotometer (Aquila NKD 7000V) with a 150 Watt Xe arc lamp as a light source in the range 200-1200 nm. Thin film samples are analyzed using Thermo Fisher K-Alpha electron spectrometer with Al Kα X-rays (monochromatic), with a flood gun used to charge neutralization under the base pressure 10^{-7} Pa for XPS analysis.

3. Results and Discussion

3.1 Microstructural Characterization

3.1.1 X-Ray Diffraction Analysis

Figure 1 a shows the XRD patterns of cerium oxide thin films with different mole concentrations deposited at an optimized substrate temperature (T_s) 400^{o}C.

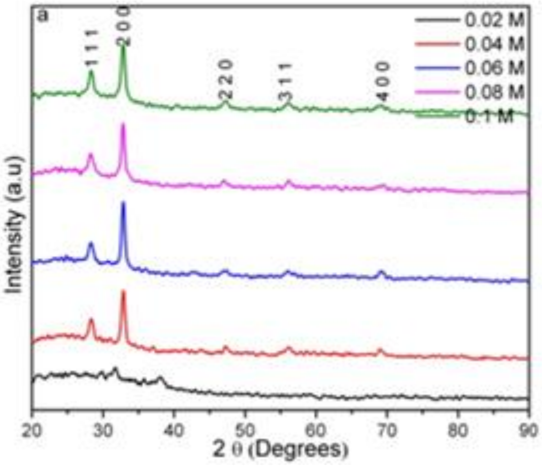

Fig.1 (a): XRD Patterns of spray coated cerium oxide thin films with different mole concentrations

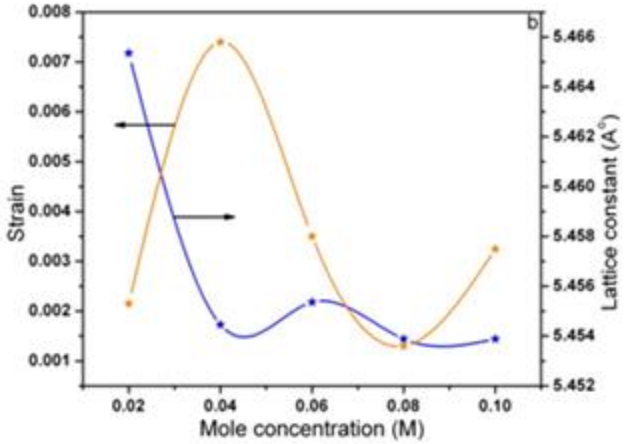

Fig.1 (b)

The presence of diffraction peaks indicates the single phase polycrystalline nature of cubic fluorite structure with preferred orientation along (200) direction [30]. The minority peaks are observed at 2θ= 28.34, 47.12, 56.35 and 69.31^o corresponds to (111), (220), (311) and (400) hkl planes respectively. The XRD peaks are compared to JCPDS data file (number 34-0394). Significant sharpening of the peaks indicates the increase of crystalline size with increasing mole concentrations upto 0.8 M and then decreases. The lattice parameter a is calculated using equation (1) for the sprayed cerium oxide films

.

$$\frac{1}{d^2} = \left[\frac{h^2 + k^2 + l^2}{a^2}\right] \qquad (1)$$

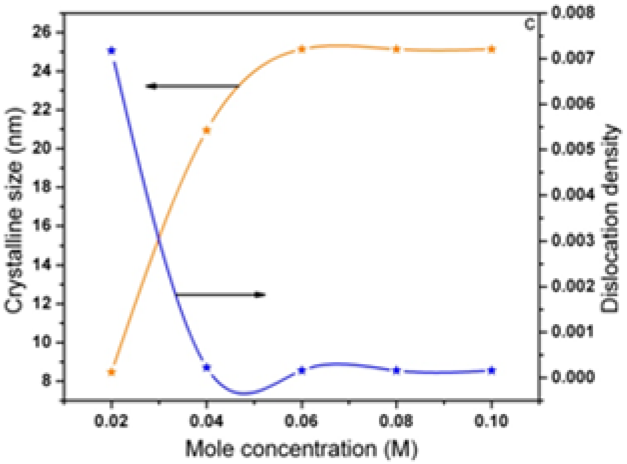

Fig.1 (c)

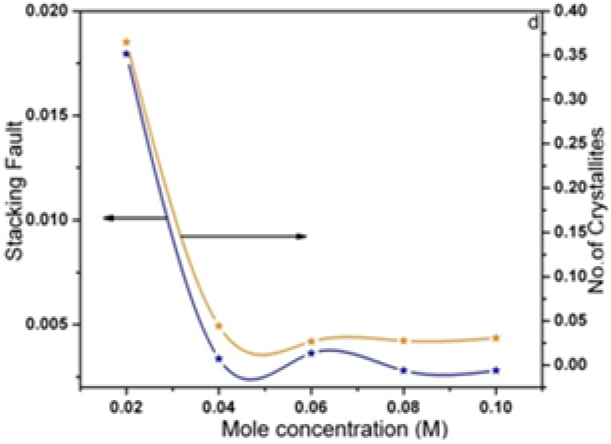

Fig.1 (d)

Fig.1 (b-d): Variations of lattice constant and strain, crystalline size and dislocation density, stacking fault and number of crystallites of cerium oxide thin films with different mole concentrations.

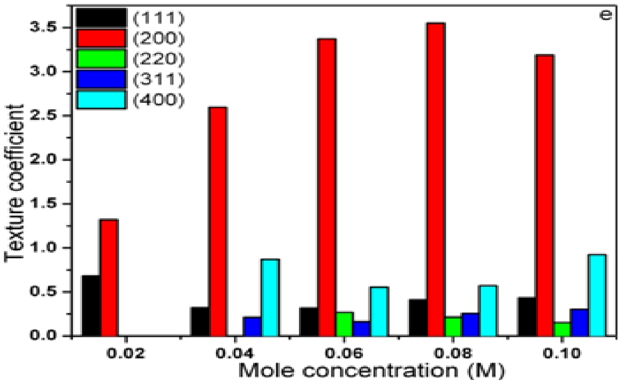

Fig.1 (e): Variation of texture coefficient with different mole concentrations of cerium oxide thin films

The variation of lattice constant (a) and strain (ε) of cerium oxide films are shown in Fig. 1b. It is observed that the lattice constant is found to be varied from 0.5416 to 0.5465 nm with the change in mole concentrations from 0.02 M to 0.1 M. The variation of average crystalline size (D) and dislocation density (δ) of cerium oxide thin films with different mole concentrations are shown in Fig. 1c. The average crystalline size is found to be varied in the range 5-30 nm with different mole concentrations 0.02 M to 0.1 M. The maximum crystalline size of the sprayed cerium oxide films is found to be 30.1 nm prepared at 0.08 M. The crystallization levels of the films are good because of their small dislocation density (δ) and lower micro strain (ε) values that represent the amount of defects in the film. The variation of stacking fault and number of crystallites of cerium oxide thin films are shown in Fig. 1d. It shows the minimum number of crystallites is observed at 0.08 M as indicated by decrease of FWHM. The texture coefficient is calculated using equation (2);

$$T_c(h_ik_il_i) = \frac{I_o(h_ik_il_i)}{I_s(h_ik_il_i)}\left[\frac{1}{N}\sum_{i=1}^{n}\frac{I_o(h_ik_il_i)}{I_s(h_ik_il_i)}\right]^{-1} \qquad (2)$$

Where, I_o is the observed intensity of $[h_ik_il_i]$ plane, $I_s$is the standard intensity of $[h_ik_il_i]$ plane and N is the total number of measured reflections. The calculated texture coefficient values present some important structural information. The variation of texture coefficient calculated for the crystal planes (111), (200), (220), (311) and (400) with mole concentrations of sprayed cerium oxide films are shown in Fig. 1e.

The increase in preferential orientation is attributed with the increased number of grains along the plane. The high value of T_c (200) indicates the maximum preferred orientation of the films along the (002) plane at 0.08 M, and lack of grains along (111) and (220) planes [31]. The increase in texture coefficient (T_c) with mole concentrations (0.08 M) indicates an improvement in the crystallinity of the cerium oxide films. These structural parameters are calculated and listed in table 1.

Table 1: Structural parameters of cerium oxide thin films

Mole concentration	2 theta (°)		d-spacing (A°)		hkl	Crystalline size (nm)	No. of crystallites	Lattice constant (nm)	Texture Coefficient
	standard	observed	standard	observed					
0.02	28.555	28.369	3.1234	3.1460	111	10.1	0.3649	0.5449	0.6821
	33.082	32.834	2.7056	2.7276	200	5.4	2.9876	0.5455	1.3178
0.04	28.555	28.389	3.1234	3.1438	111	15.5	0.1085	0.5446	0.3214
	33.082	32.770	2.7056	2.7329	200	20.9	0.0444	0.5465	2.5979
	56.335	56.174	1.6318	1.6374	311	11.4	0.2691	0.5435	0.2102
	69.402	68.974	1.3530	1.3614	400	20.3	0.0487	0.5448	0.8703
0.06	28.555	28.357	3.1234	3.1473	111	15.5	0.1123	0.5451	0.3170
	33.082	32.818	2.7056	2.7290	200	25.1	0.0265	0.5458	3.3733
	47.479	47.029	1.9134	1.9322	220	16.7	0.0925	0.5465	0.2678
	56.335	56.082	1.6318	1.6399	311	13.1	0.1852	0.5439	0.1614
	69.402	69.178	1.3530	1.3569	400	10.0	0.4212	0.5427	0.5520
0.08	28.555	28.283	3.1234	3.1554	111	12.4	0.2268	0.5465	0.4086
	33.082	32.845	2.7056	2.7268	200	25.1	0.0274	0.5453	3.5527
	47.479	47.088	1.9134	1.9299	220	30.1	0.0158	0.5458	0.2131
	56.335	56.155	1.6318	1.6379	311	10.1	0.4139	0.5432	0.2555
	69.402	69.410	1.3530	1.3540	400	9.9	0.4402	0.5416	0.5699
0.1	28.555	28.317	3.1234	3.1517	111	20.7	0.0547	0.5458	0.4344
	33.082	32.821	2.7056	2.7287	200	25.1	0.0306	0.5457	3.1899
	47.479	47.259	1.9134	1.9217	220	8.9	0.6698	0.5435	0.1509
	56.335	56.145	1.6318	1.6382	311	22.8	0.0409	0.5433	0.3017
	69.402	69.273	1.3530	1.3564	400	16.0	0.1168	0.5425	0.9229

3.1.2 Surface morphology analysis

Figure 2 displays the SEM images of cerium oxide thin films prepared with different mole concentrations deposited at an optimized substrate temperature. It indicates the films are uniform, crack-free, smooth and well adherent to the substrates. It shows the prepared films are granular structure having sparingly adequate tiny spherical like particles with an average size of 52 nm [23]. At lower concentration, films are rather rough surface upto 0.04 M and then smoothness of the films increases upto 0.08 M and then some cracks are appeared in the surface at higher concentration. The smoothest surface is obtained at 0.08 M.

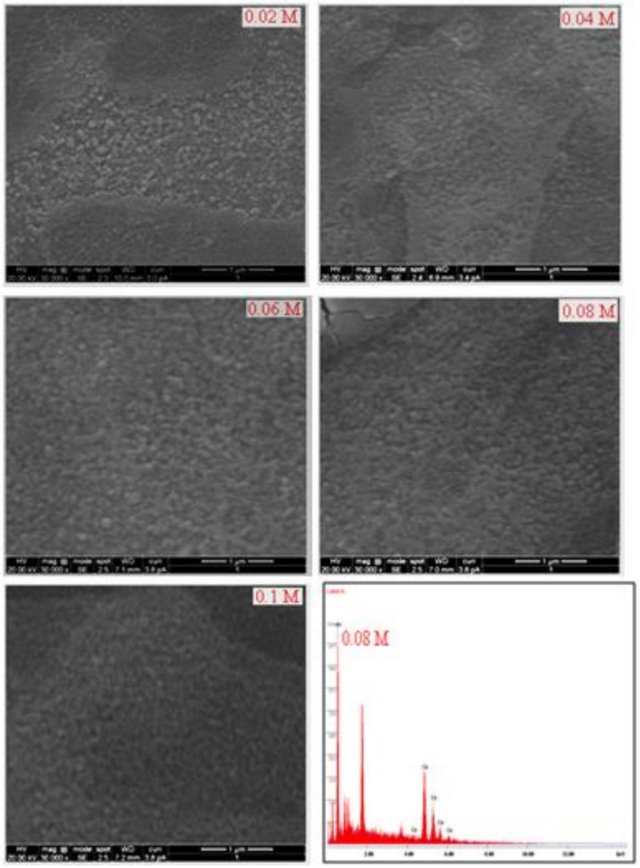

Fig.2: SEM-EDS analysis of spray coated cerium oxide thin films with different mole concentrations.

EDS analysis confirm the presence of Ce, O and Si atoms in the prepared films.

Fig. 3 depicts the tapping mode AFM image of cerium oxide thin films prepared at 0.08 M. The figure exhibits nicely separated conical columnar microstructure with measured roughness (area Ra = 12.25 nm) and (area RMS = 15.38 nm). The results are in good agreement with SEM observations with a uniform and dense morphology.

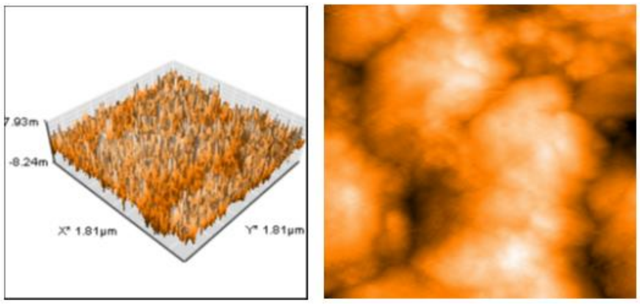

Fig.3: AFM 2D & 3D images of spray coated cerium oxide thin films prepared at 0.08 M.

From these results, it is corroborated that the particle sizes ranged from 10 to 50 nm in diameter as a result of nucleation and coalescence of spray droplets during deposition process [32]. Surface roughness is directly proportional to the gas sensitivity of the film since larger roughness results in larger interface area with the gaseous species. This is a manifestation of the importance of surface-to-volume ratio in gas sensing applications.

3.1.3 FT-IR Analysis

The IR study gives the information about phase composition as well as the way oxygen is bound to the metal ions. Figure 4 shows the FTIR spectra of cerium oxide thin films prepared with different mole concentrations.

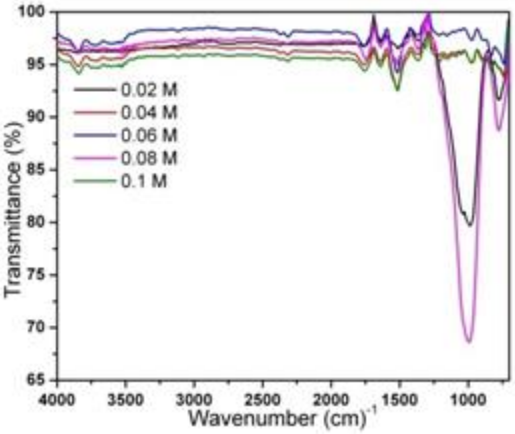

Fig.4: FT-IR spectra of spray coated cerium oxide thin films with different mole concentrations.

It is observed that the CeO_2 thin films show a group of strong intense bands at 992, 1523 and 3835 cm^{-1}, which may be attributed to the presence of υ(O-H….H) stretching mode, bending mode of hydroxyl groups of absorbed water and υ(O-H) mode of (H-bonded) water molecules respectively. The lower intensity peaks at 2928, 2371 and 2313 cm^{-1} are assigned to the υ(C-H) mode of residual organic moieties and υ(C-O) stretching mode of vibrations. The relatively broad peak is observed at 3719 cm^{-1} attributed to the υ(CH_3) mode of organic group. The broad bands observed at 1639 and 771 cm^{-1} are due to the envelope of (Ce=O) terminal stretching and phonon band of metal oxide (Ce-O) network respectively [3]. The carbonation of ceria films is unavoidable in ambient atmosphere which is diminished at an optimized mole concentration 0.08 M.

3.2 Optical properties

3.2.1 PL Analysis

Figure 5 shows the PL spectra of cerium oxide thin films prepared with different mole concentrations.

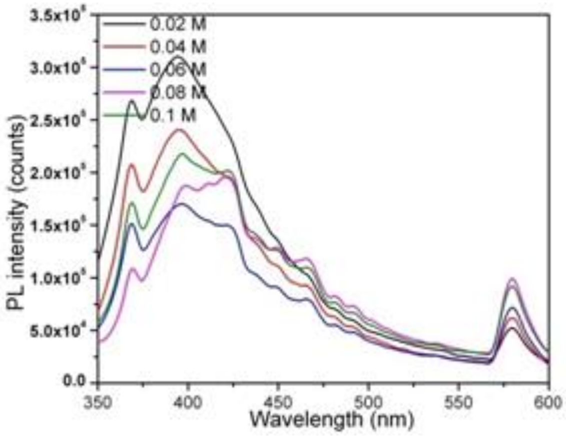

Fig.5: PL spectra of spray coated cerium oxide thin films with different mole concentrations.

Two consistent sharp and broad peaks observed at 425 and 579 nm correspond to indigo and yellow emission in the visible region. Minority peaks are observed at 368, 394, 467, 483 and 492 nm in the visible region. The emission bands ranging from 400-500 nm for CeO_2 thin films are attributed to the hopping from different defect levels exist as Ce4f to O2p band. It suggests that the strong emission of the CeO_2 films at 467 nm is related to the abundant defects which are helpful for fast oxygen transportation. The defects energy levels between Ce4f and O2p are dependent on the temperature and density of defects in the films. The broad peak at 394 nm could be due to either 5d to 4f or 4f to valence band energy gap of 3.1 eV obtained from optical absorption measurements on CeO_2 reported in the literature [33]. It reveals the strong and sharp emission bands are observed for the films prepared at 0.08 M compared with other films.

3.2.2 UV-ViS analysis

Figure 6a shows the optical absorbance spectra of cerium oxide thin films prepared at various mole concentrations. From this Figure, some of the intensity of the peaks are shifted towards the UV region. High value of absorbance in UV region is observed and the same is found to be decreased sharply with increasing wavelength and becomes almost constant towards the visible region. The absorbance increases with increasing mole concentration upto 0.06 M and then decreases due to the increase of densification pore size and oxygen additives in the prepared films.

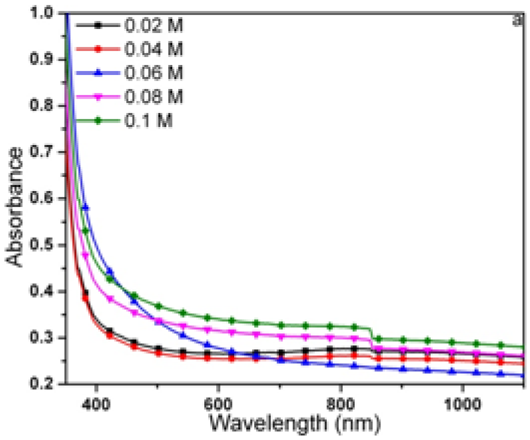

(a)

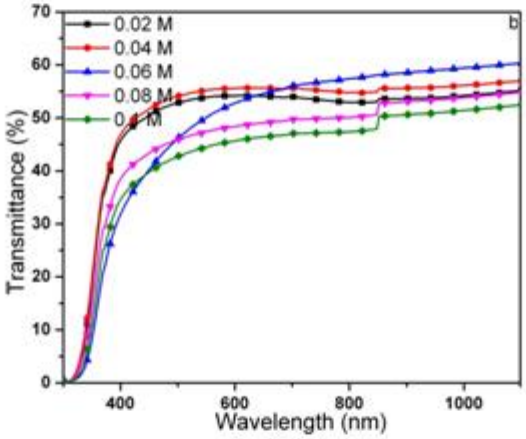

(b)

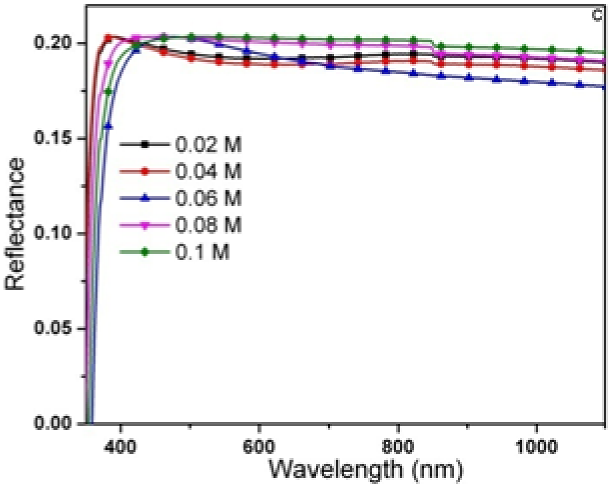

(c)

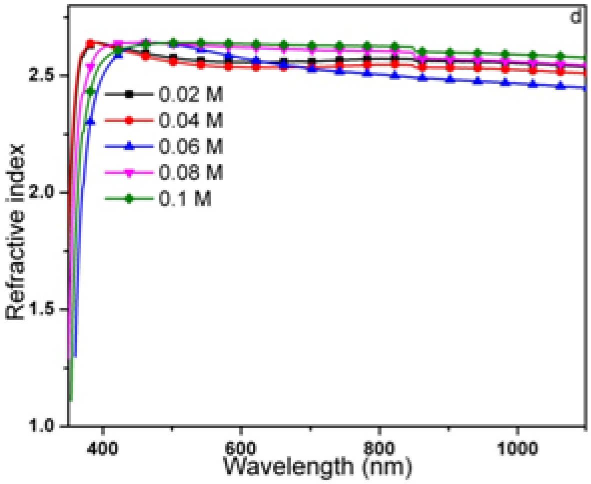

(d)

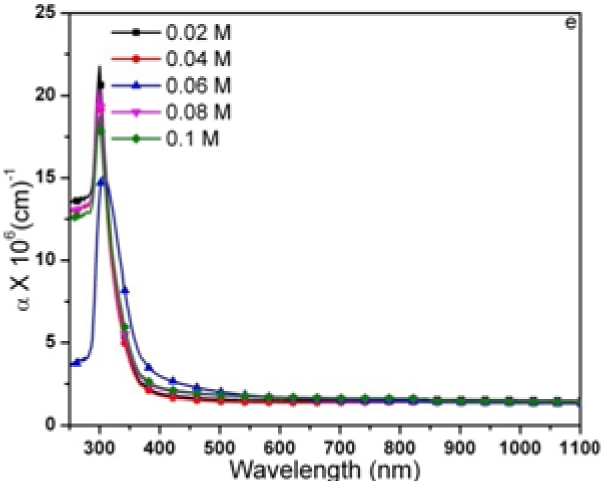

(e)

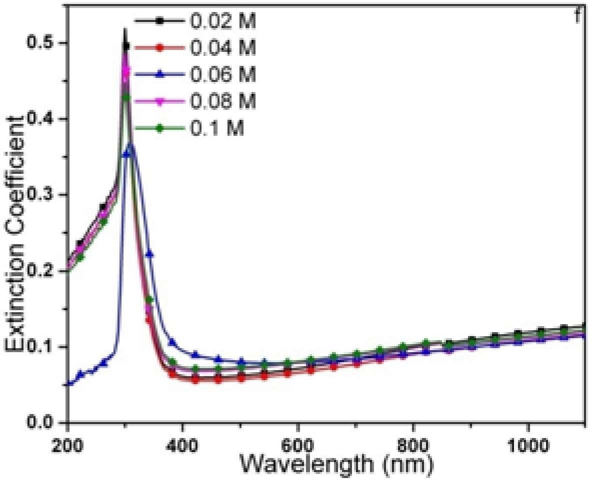

(f)

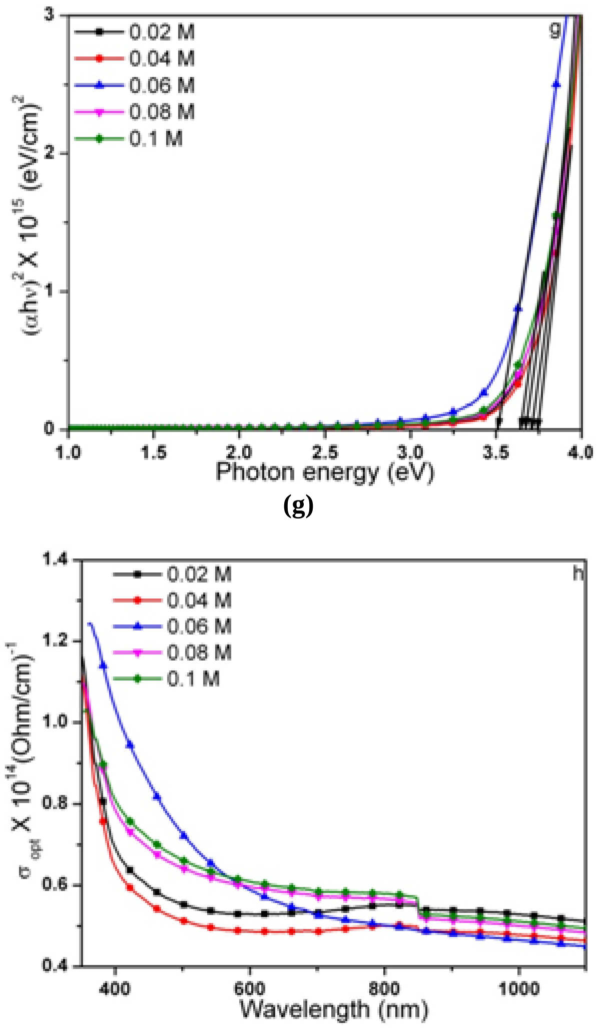

(g)

(h)

Fig.6: UV-ViS spectra of spray coated cerium oxide thin films with different mole concentrations.

Figure 6b shows the transmittance spectra of cerium oxide thin films. It shows that the transmittance decreases to zero in the UV region, the same increases up to 60% in the visible region and remains almost constant in the NIR region.

The transmittance decreases with increasing mole concentration due to the presence of covalent bonds between cerium and an oxygen additive which decreases the transmittance of the incident light especially at the shortest wavelengths. The electrons in the outer orbits have travelled to the higher energy levels and have occupied vacant positions of energy bands. Thus, a part of incident light does not penetrate through it [34]. The maximum transmittance is observed (nearly 60%) in 0.06 M sample due to impurities present in the precursor and thickness. Reflectance also decreases with increasing mole concentration up to 0.06 M and then increases as shown in Figure 6c. The refractive index is calculated using the following equation,

$$n = \frac{1+R}{1-R} \pm \sqrt{\frac{4R}{(1-R)^2} - k^2} \tag{3}$$

Where, R is the reflectance and k is the extinction coefficient. The refractive index of the films is estimated from spectral transmittance and reflectance data for different mole concentrations and is given in Figure 6d. It is shown from this figure that the refractive index increases from 2.53 to 2.63 as the mole concentration is increased from 0.02 M to 0.1 M. The increase in refractive index with mole concentration is mainly due the increase of packing density, thickness and low extinction coefficient. The gradient of the absorption coefficient is from high photon energy to low photon energy. This means that the possibility of electron transition is little, as the energy is not enough to move the electron from the valence band to the conduction band $(h\upsilon<Eg)$. It is anticipated that indirect transition of electron occurs at low absorption coefficient and the electronic momentum is maintained with assistance of photon. The energy of incident photon is greater than the forbidden energy gap. The absorption coefficient is calculated using the following equation,

$$\alpha = \frac{\ln(1/T)}{t} \tag{4}$$

Where, α is the absorption coefficient, T is the transmittance and t is the thickness. The dependence of absorption coefficient of films on wavelength is shown in Figure 6e. It indicates that the absorption coefficient increases upto certain values of wavelength in UV region then exponentially decreases and finally becomes constant in the visible and NIR region. The extinction coefficient is calculated using the following relation,

$$k = \frac{\alpha\lambda}{4\pi} \tag{5}$$

Where, α is the absorption coefficient and λ is the wavelength. The estimated value of extinction coefficient of the films shows that (Figure 6f) it increases upto certain values of wavelength in UV region and then exponentially decreases and finally becomes constant in the visible and NIR region. The optical bandgap is calculated by:

$$(\alpha h\nu)^n = B(h\nu - E_g) \tag{6}$$

Where, α is the absorption coefficient, hν is the photon energy, B is a constant and E_g is the optical bandgap. In order to determine the values of optical bandgap, $(\alpha h\nu)^n$ vs hν curves have been plotted for the prepared films and the values of n = 1/2, 3/2, 2 and 3 for direct allowed, direct forbidden, indirect allowed and indirect forbidden transitions respectively. The values of the tangents intercepting the energy axis give the values of optical band gap as shown in Fig. 6g. The calculated optical bandgap is found to be in the range 3.50 to 3.74 eV for indirect allowed transitions. These values are compared to earlier works [35]. The optical conductivity is related to velocity of light by following equation,

$$\sigma_{OPT} = \frac{nc\alpha}{4\pi} \tag{7}$$

Where, n is refractive index, c is velocity of light and α is absorption coefficient. The optical conductivity decreases suddenly at 300 nm wavelength as shown in Figure 6h. It is observed that the optical conductivity decreases with increasing mole concentration upto 0.04 M and then increases due to the increase of the contribution of electron transition between valance band and conduction band, which led to reduction of energy gap (Figure 6g) as a result of sit level generation. The conductivity becomes constant after 600 nm. The calculated optical conductivity is in the range 4.8911 X 10^{13} to 6.1699 X 10^{13} $(\text{Ohm/cm})^{-1}$. The optical parameters are calculated and listed in table 2.

Table 2: Optical parameters of cerium oxide thin films

Mole concentration (M)	Absorption coefficient X 10^6 (cm^{-1})	Extinction coefficient	Refractive index	Bandgap energy (eV)	Thickness (nm)	Optical conductivity X 10^{13} $(ohm/cm)^{-1}$
0.02	1.5159	0.06634	2.56	3.71	384	5.3460
0.04	1.4082	0.06163	2.54	3.74	408	4.9386
0.06	1.7990	0.07874	2.60	3.51	422	6.4264
0.08	1.7098	0.07483	2.62	3.67	436	6.1454
0.1	1.7481	0.07651	2.64	3.64	463	6.3042

3.3 Elemental analysis

XPS technique is used to determine the stoichiometry, purity and chemical state of the prepared samples. Based on the survey spectrum of the cerium oxide thin films (Fig. 7a) only cerium, oxygen, sodium (originated from the substrate) and surface carbon (due to air contamination and CO/CO_2 adsorption on the surface) is detected on the films with no other surface impurities.

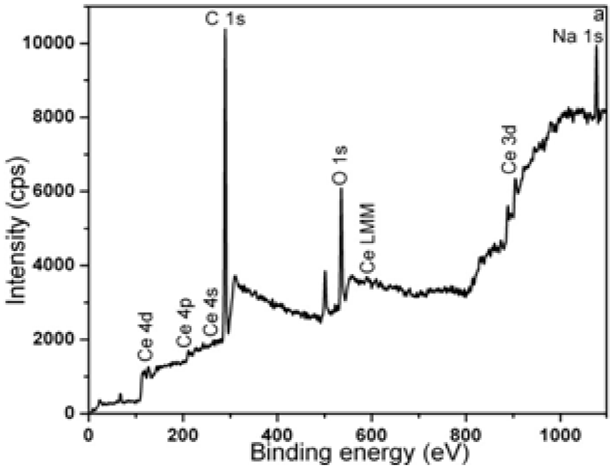

(a)

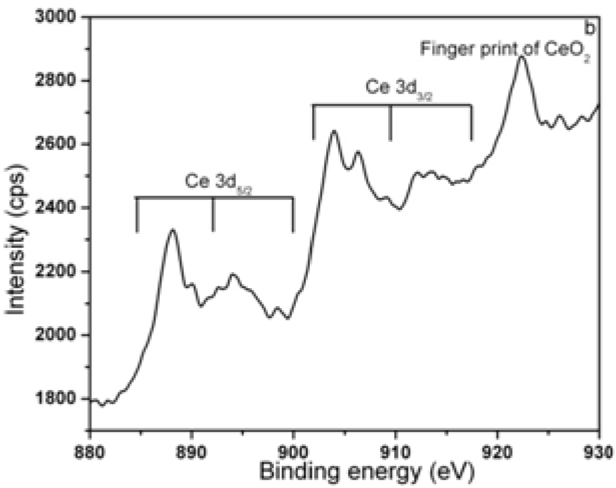

(b)

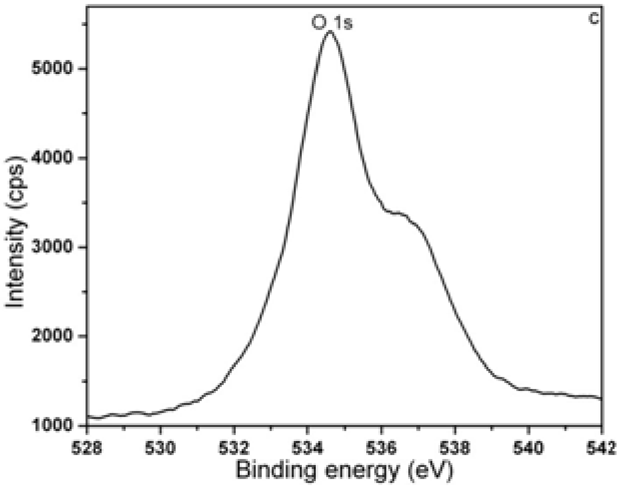

(c)

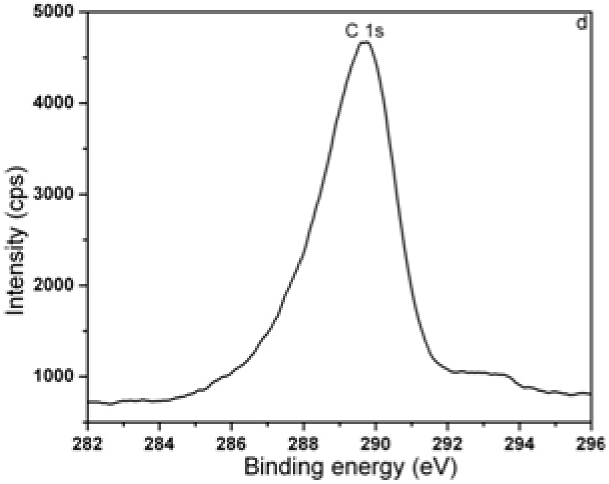

(d)

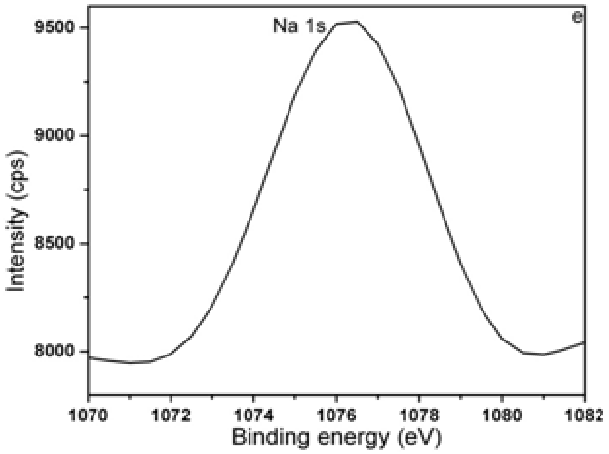

(e)

Fig.7: XPS spectra of spray coated cerium oxide thin films prepared at 0.08 M.

The Ce3d core level spectrum (Fig. 7b) consists of three pairs of $3d_{3/2}$-$3d_{5/2}$ spin-orbit-split doublets representing different 4f configurations in the photoemission final state and arising from 4f hybridization in both the initial and final states. It can be individually deconvoluted into three pairs of $3d_{5/2}$ and $3d_{3/2}$ spin–orbit components describing the $Ce^{4+} \leftrightarrow Ce^{3+}$ electronic transitions in the binding energies 888.17, 894.16, 898.48, 903.98, 906.29 and 916.42 eV. The first three peaks correspond to $Ce3d_{5/2}$ and last three peaks correspond to $Ce3d_{3/2}$. These results indicate the presence of pure CeO_2 and less impurity is presented. This is further supported by the presence of peak at 922.43 eV, which is considered as a fingerprint of the CeO_2 phase [36]. Fig. 7 c-e shows the O 1s, C 1s and Na 1s core level spectra of CeO_2 thin films. The higher binding energy feature at around 534.2 eV suggest the presence of Ce^{4+} related surface defects where oxygen occupies additional lattice sites and the lower energy component feature at around 536.8 eV correspond to oxide ions in a defective Ce_2O_3 formation of hydroxyl groups on the surface or oxygen chemisorbed on the surface. Small amount of carbon atom is absorbed from atmosphere at binding energy 291.98 eV (due to air contamination and CO/CO_2 adsorption on the surface) according to FT-IR results.

Table 3: Elemental composition of cerium oxide thin films

Elements	Binding energy (eV)	Electron configuration		Compounds	Peak components	Percentage (%)
		Initial state	Final state			
Ce	888.17 890.04 894.16	$Ce\ 3d^{10}4f^0$-$O2p^6$ $Ce\ 3d^{10}4f^0$-$O2p^6$ $Ce\ 3d^{10}4f^0$-$O2p^6$	$Ce\ 3d^9 4f^3$-$O2p^4$ $Ce\ 3d^9 4f^2$-$O2p^5$ $Ce\ 3d^9 4f^1$-$O2p^6$	Ce^{4+} (CeO_2)	Ce $3d_{5/2}$	34.81
	903.93 906.43 917.82	$Ce\ 3d^{10}4f^1$-$O2p^6$ $Ce\ 3d^{10}4f^1$-$O2p^6$ $Ce\ 3d^{10}4f^1$-$O2p^6$	$Ce\ 3d^9 4f^0$-$O2p^6$ $Ce\ 3d^9 4f^1$-$O2p^5$ $Ce\ 3d^9 4f^2$-$O2p^4$	Ce^{3+} (Ce_2O_3)	Ce $3d_{3/2}$	19.80
O	534.61 536 536.71 537.21	-	-	CeO_2 Ce_2O_3 C=O, C-O OH, $-No_3$, R-O-R	O 1s	11.87
C	289.69 293.59	-	-	C-N CO_3	C 1s	19.23
Na	1076.29	-	-	-	Na 1s	14.26

Small amount of sodium atom is originated from substrate surface at binding energy 1076.54 eV [37]. Composition of all the elements are calculated and listed in table 3 according to EDS results.

4. Conclusion

Nanocrystalline cerium oxide thin films with dense microstructure and free of cracks have been successfully deposited on glass substrates using NSP technique. All the films exhibit single phase crystalline and cubic fluorite structure with preferred orientation along (200) direction. The obtained maximum crystalline size is 30.1 nm prepared at 0.08 M. When mole concentration exceeds 0.08 M, some of the particles are broken and form cracks in the surface due to the agitation of particles and shrinkage of spray droplets. Crack free and smooth surfaces are obtained at 0.08 M. It also exhibits nicely separated conical columnar microstructure with measured roughness of 15.38 nm. FT-IR confirm the presence of phonon band of the metal oxide (Ce-O) and terminal stretching vibration (Ce=O). The carbonation peaks are diminished at optimized mole concentration 0.08 M. PL spectra revealed the presence of indigo-yellow emission peaks centered at 425 and 579 nm in the visible region. The peak observed at 394 nm due to charge transfer between 5d and 4f. The calculated refractive index and optical conductivity is found to be in the range 2.53 to 2.33 and 4.8911×10^{13} to 6.1699×10^{13} $(ohm/cm)^{-1}$. XPS analysis exhibits the presence of Ce, O and C in the prepared films. It shows the dominant occurrence of Ce^{4+}, minority occurrence of Ce^{3+} and small amount of C absorbed from air. From these results, films prepared at 0.08 M shows better crysrallalanity, smooth surface, broad emission, high transmittance, high optical conductivity and less impurities compared to other films prepared from 0.02 to 0.1 M. The film can be applied to optoelectronic devices due to the high optical conductivity, electrochemical devices due to its large charge recombination and gas sensors owing to its smooth surface and large surface area

References

[1] M. Mogensen, N. M. Sammes, G. A. Tompsett, *Solid State Ionics* **129**, 63-94 (2000).

[2] R. I. Walton, Progress in Crystal Growth and *Characterization of Materials* **57**, 93-108 (2011).

[3] A. K. Bhosale, N. L. Tarwal, P. S. Shinde, P. M. Kadam, R. S. Patil, S. R. Barman, P. S. Patil, *Solid State Ionics* **180**, 1324-1331 (2009).

[4] C. Y. Chen, T. K. Tseng, S. C. Tsai, C. K. Lin, H. M. Lin, *Ceramics International* **34**, 409-416 (2008).

[5] B. B. Patil, S. H. Pawar, *Applied Surface Science* **253**, 4994-5002 (2007).

[6] A. Samson Nesaraj, I. Arul raj, R. Pattabiraman, *Indian Journal of Chemical Technology*, **14**, 154-160, (2007).

[7] V. Thangadurai, W. Weppner, *Electrichimica Acta* **49**, 1577-1585 (2004).

[8] Lin Liu, Gap-Yong Kim, Abhijit Chandra, *Journal of Power Sources* **195**, 7046-7053 (2010).

[9] A. K. Bhosale, P. S. Shinde, N. L. Tarwal, R. C. Pawar, P. M. Kadam, P. S. Patil, *Electrochimica Acta* **55**, 1900-1906 (2010).

[10] T. Petrisor, V. Boffa, G. Celentano, L. Ciontea, F. Fabbri, U. Gambardella, S. Ceresara, P. Scardi, *IEEE Trans. App. Super.* **9**, 2256-2259 (1999).

[11] F. E. Ghodsi, F. Z. Tepehan, G. G. Tepehan, *Optical Materials* **31**, 63-67 (2008).

[12] T. Yoshino, H. Masuda, *Solid State Ionics* **165**, 123-129 (2003).

[13] N. Imanaka, T. Masui, H. Hirai, G. Adachi, *Chem. Mater.* **15**, 2289-2291 (2003).

[14] I. T. Liu, M. H. Hon, L. G. Teoh, *Ceramics International* **40**, 4019-4024 (2014).

[15] C. Li, R. Chen, X. Zhang, S. Shu, J. Xiong, Y. Zheng, W. Dong, *Materials Letters* **65**, 1327-1330 (2011).

[16] S. Kim, S. H. Cho, S. R. Choi, M. C. Oh, J. H. Jang, P. K. Song, *Thin Solid Films* **517**, 4061-4064 (2009).

[17] Syed M. Bukhari, Javier B. Giorgi, *Sensors and Actuators B* **156**, 524-537 (2011).

[18] S. M. A. Durrani, M. F. Al-Kuhaili, I. A. Bakhtiari, *Sensors and Actuators B* **134**, 934-939 (2008).

[19] S. Somacescu, P. Osiceanu, J.M. Calderon Moreno, L. Navarrete, J. M. Serra, *Microporous and Mesoporous Materials* **179**, 78-88 (2013).

[20] A. M. Torres-Huerta, M. A. Dominguez-Crespo, S. B. Brachetti-Sibaja, H. Dorantes-Rosales, M. A. Hernandez-Perez, J. A. Lois-Correa, *Journal of Solid State Chemistry* **183**, 2205-2217 (2010).

[21] Jong HoonJoo, Gyeong Man Choi, *Solid State Ionics* **177**, 1053-1057 (2006).

[22] Irena kozjekskofic, Sasosturm, Miran Ceh, Natasa Bukovec, *Thin Solid Films* **422**, 170-175 (2002).

[23] Ming Wei, K. L. Choy, *Journal of Crystal Growth* **284**, 464-469 (2005).

[24] H. W. Song, C. S. Lee, D. G. Kim, K. No., *Thin Solid Films* **368**, 61-66 (2000).

[25] P. Nowakowski, S. Villain, K. Aguir, J. Guerin, A. Kopia, J. Kusinski, F. Guinneton, J. R. Gavarri, *Thin Solid Films **518***, 2801-2807 (2010).

[26] V. Shelukhin, I. Zon, E. Watchtel, Y. Feldman, I. Lubomirsky, *Solid State Ionics* **211**, 12-19 (2012).

[27] J. Im, I. Park, D. Shin, *Ceramics International* **38**, 2051-2058 (2012).

[28] Nikolaous I. Karageorgakis, Andre Heel, Thomas Graule, Ludwig J. Gauckler, *Solid State Ionics* **192**, 464-471 (2011).

[29] R. Suresh, V. Ponnuswamy, R. Mariappan, N. Senthilkumar, *Ceramics International* **40**, 437-445, (2014).

[30] J. de Souza, A. G. P. da Silva, H. R. Paes, *J. Mater. Sci.* **18**, 951-956 (2007).

[31] R. Suresh, V. Ponnuswamy, R. Mariappan, *Applied Surface Science* **273**, 457-464 (2013).

[32] I. Uslu, A. Aytimur, M.K. Ozturk, S. Kocyigit, *Ceramics International* **38**, 4943-4951 (2012).

[33] A. GiardiniGuidoni, C. Flamini, F. Varsano, M. Ricci, R. Teghil, V. Marotta, T.M. Di Palma, *Applied Surface Science* **154-155**, 467-472 (2000).

[34] F. A. Mustafa, *Physical Sciences Research International* **1**, 1-9 (2013).

[35] S. Debnath, M.R. Islam, M.S.R. Khan, *Bulletin Material Science* **30**, 315-319 (2007).

[36] F. Pagliuca, P. Luches, S. Valeri, *Surface Science* **607**, 164-169 (2013).

[37] M. Yousefi, R. Azimirad, M. Amiri, A. Z. Moshfegh *Thin Solid Films* **520**, 721-725 (2011).